

A unified microscopic picture of cation and anion migration in MAPbI₃

Viren Tyagi,[†] Geert Brocks,^{†,‡} and Shuxia Tao^{*,†}

[†]*Department of Applied Physics and Science Education, Eindhoven University of Technology, 5600 MB, Eindhoven, The Netherlands*

[‡]*Computational Chemical Physics, Faculty of Science and Technology and MESA+ Institute for Nanotechnology, University of Twente, 7500 AE, Enschede, The Netherlands*

E-mail: s.x.tao@tue.nl

Abstract

Passivating defects and restricting defect mobilities in halide perovskites to increase device lifetimes has become a main field of research. Modeling structure and mobility of point defects is an essential contribution to this endeavor. We employ molecular dynamics, based on neural network potentials trained on density functional theory data, to model ion migration in MAPbI₃ triggered by I and MA vacancies or interstitials. Most of these species diffuse rapidly at room temperature, with migration barriers between 0.15 and 0.20 eV. MA interstitials are highly mobile despite their molecular nature, owing to a concerted migration mechanism involving multiple MA ions. No evidence of MA vacancy migration is obtained. Whereas diffusion of I-related defects appreciably depends on their charge state, diffusion of MA defects does not. These results revise the conventional picture of ion transport in hybrid perovskites and highlight the role of collective molecular motion in enabling fast ionic migration.

Introduction

Hybrid organic-inorganic metal halide perovskites have shown great potential for application in photovoltaic and light-emitting devices.¹ The materials allow for optimization of optoelectronic properties through chemical compositional flexibility and low temperature solution processing.^{2,3}

Halide perovskites are soft materials, however, where defects in the crystal lattice are relatively easily formed.^{4,5} Whereas most of these defects do not seem to alter the basic optical and electronic parameters much, they can trigger chemical decomposition and degradation.⁶ Defects facilitate ion migration through the material to surfaces, grain boundaries, and interfaces with electrodes, where degradation reactions are likely to take place.^{7,8} Passivating defects or limiting defect mobilities in order to enlarge device lifetimes has become a main field of research in halide perovskites.^{9,10} Identifying the character and mobility of the relevant migrating defects is then the first essential step.

A majority of experimental studies on ion transport in halide perovskites focus on MAPbI₃ (MA = CH₃NH₃⁺, methylammonium) as the prototype halide perovskite material. Assuming that the observed ion migration behaviors relate to intrinsic properties of bulk MAPbI₃, the prime vehicles for diffusion should be point defects, i.e., single ion interstitials and/or vacancies, rather than extended or compound defects.¹¹ It is generally agreed upon that Pb interstitials and vacancies are immobile at room temperature, which leaves I and/or MA defects as possibilities.^{12,13}

Halide anion migration receives most attention in MAPbI₃. Temperature-dependent measurements allow for the extraction of migration barriers, but the numbers extracted from different experiments show a considerable spread. Experi-

ments cover (temperature-dependent) conductivity, capacitance or photoluminescence,^{14–25} transient ion drift,²⁶ impedance and deep-level transient spectroscopy,^{27–31} and find diffusion barriers ranging from 0.10 to 0.68 eV. Some of these experiments also report barriers for the diffusion of MA cations, with again a considerable spread in numbers from 0.18 to 0.94 eV. Per study the numbers for the migration barriers of MA cations tend to be somewhat larger than those for the I anions, but both species can be mobile.

Whereas charge states, energy levels, and diffusion coefficients of migrating species are experimentally accessible, the nature and composition of the actual migrating defects are less so. Studies therefore use density functional theory (DFT) calculations as support. The workhorse method for extracting migration barriers is based on transition state theory (TST) and finding a lowest-energy path following the nudged elastic band (NEB) method, for instance. This approach suffers from the difficulty of finding such a path in a soft material such as MAPbI₃, where in fact many such paths may compete and contribute, as the low symmetry of the MA cation enables multiple energetically competitive configurations.^{32,33} Values reported for the migration barriers range from 0.08 to 0.58 eV for the iodide vacancy, 0.08 eV for the iodide interstitial, and 0.46 to 0.96 eV for the MA vacancy.^{15,34–39} We do not know of reports on such a calculation on the MA interstitial, although its formation energy is predicted to be only moderate to low.^{40,41}

Migration rates or diffusion coefficients cannot be extracted directly from a NEB calculation. This is possible using molecular dynamics (MD) simulations. Molecular dynamics samples all relevant migration pathways and configurations. It allows for direct simulations of ion diffusion at preset temperatures, giving access to diffusion rates and barriers. The Achilles heel of MD is the force field used in the simulations. From a parametrized analytical force field, migration barriers of 0.1 and 0.55 eV have been extracted for the iodide vacancy and interstitial, respectively.^{42,43} The accuracy of such force fields is debated, however.³³ A breakthrough has been achieved in recent years in the form of machine learned force fields (MLFFs), which allow for MD simulations using force fields

at DFT accuracy.^{44–46} By selecting the DFT data on which the MLFFs are trained, it is possible to target MD simulations toward specific charge states of the migrating species.^{47,48}

We use MD based on MLFFs to model ion migration in MAPbI₃ triggered by I anion vacancies or interstitials, and by MA cation vacancies or interstitials. We find all species to be extremely mobile, except for the MA vacancy. The mobility of halide anion defects, vacancies and interstitials, is comparable to that found in the all inorganic compounds CsPb(I_xBr_{1-x})₃; $x = 0, \dots, 1$,^{47,49} leading to the conclusion that the A cation species in the perovskite structure does not affect halide motion much. Remarkably, the diffusion rate of MA interstitial cations is only slightly smaller than that of I interstitial anions. Migration of MA interstitials proceeds via a concerted motion involving the interstitials and two of its MA neighbors in the lattice. Whereas the diffusion of I-related defects very much depends on their charge state, that of MA-related defects is virtually independent of charge state. We attribute this to the fact that an MA cation interstitial or vacancy only create very shallow impurity levels that are ionized at room temperature.

Methods

Iodide and MA interstitials and vacancies have charge states I_I^- , V_I^+ , I_{MA}^+ , and V_{MA}^- , respectively, under intrinsic or mildly doped conditions.^{41,50} Results obtained from DFT calculations differ somewhat on whether vacancies or interstitials are predicted to be the dominant species under equilibrium conditions. This reflects the use of different functionals, for instance.^{40,50} The formation energy of interstitial-vacancy (Frenkel) pairs I_I^-/V_I^+ and I_{MA}^+/V_{MA}^- only weakly depends on the functional,⁴⁰ However, including Vanderwaals (VdW) interactions favors interstitials over vacancies, whereas excluding VdW interactions favors vacancies, demonstrating that VdW interactions have to be included.^{40,50}

In this paper we consider both vacancies and interstitials and train a MLFF for describing them in their most prominent charge states under intrinsic conditions. Our MLFF is based on the Alle-

gro model, which is a local E(3)-equivariant graph neural network potential (NNP), as implemented in the NequIP package.^{51,52} The datasets for training and validating the network are generated using the on-the-fly module as implemented in VASP, sampling structures from short-time scale MD runs.^{53–57} Energies, forces, and stress tensors are calculated using DFT with the SCAN+rVV10 functional.^{58,59} These are calculated for a series of structures that are sufficiently different from one another, using selection criteria based on Bayesian inference. The training and validation sets are generated using $2 \times 2 \times 2$ cubic supercells MAPbI_3 (96 atoms) containing one charged or neutral MA or I point defect. Details of the training procedure are explained in the SI note 1.

Iodide vacancies (interstitials) give acceptor (donor) levels that can be populated with electrons (holes) if the (quasi) Fermi level is very close to the conduction (valence) band, which might happen under device operating conditions.^{60,61} The same is true in principle for MA interstitials and vacancies. A NNP trained on energies and forces has no direct knowledge of electronic structure, but it is possible to select DFT data for training a neural network that are generated with a Fermi level in or close to the valence or conduction band to represent defects with modified charge states. In this way, we train separate NNPs for I_{MA}^0 and V_{MA}^0 .

The accuracy of the NNPs is explored by comparing the migration barriers along paths generated using the climbing image nudged elastic band (CI-NEB) technique with those calculated by DFT along the same paths.⁶² The computed energies are given in Figure 1, and the computed migration barriers in Table 1. The difference between the migration barriers calculated using DFT and the NNP ($|\Delta E_b^{\text{DFT}} - \Delta E_b^{\text{NNP}}|$) is less than 0.11 eV in all cases, indicating the accuracy of the NNPs. No migration events were actually observed during training for the neutral MA vacancy, V_{MA}^0 , yet the NNP accurately describes the migration barrier for this defect ($|\Delta E_b^{\text{DFT}} - \Delta E_b^{\text{NNP}}| = 0.02$ eV) (Figure 1c), demonstrating the accuracy of the NNP in extrapolating to events not explicitly included in training.

For I_{MA}^+ (Figure 1e) and I_{MA}^0 (Figure 1f), the initial and the final images do not have the same

energy, indicating that these are not the complete migration paths. It illustrates the problem of finding the lowest energy migration path in this compound. As MA cations are asymmetric and polar, the local structure around a migrating I defect allows for multiple local minima, and significant hysteresis. The details of the CI-NEB calculations are given in the SI note 2.

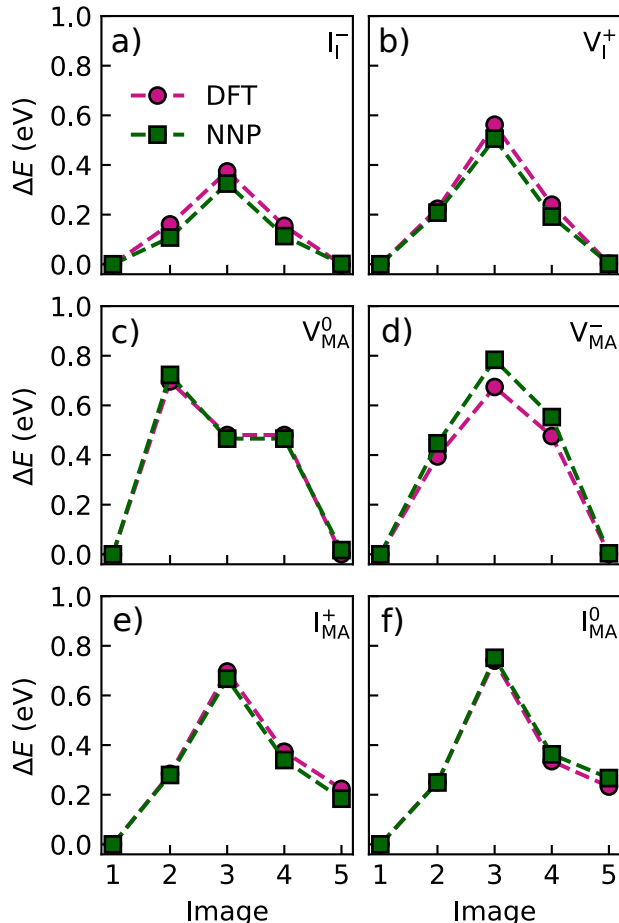


Figure 1: Energies along the NEB migration paths, calculated using DFT and the NNPs. The points are the calculated values, and the lines guide the eye; the energy of the minima is set to 0.

The forces calculated using the NNP are also compared with those calculated using DFT. This is done using structures sampled from MD simulations at 600 K performed on $6 \times 6 \times 6$ supercells of MAPbI_3 (2592 atoms) with one I or MA point defect. From these comparisons the coefficient of determination $R^2 = 0.99$ and the mean absolute error (MAE) ≤ 49.06 meV/Å. Specifically for the forces on atoms in the defect environment we

find $R^2 \geq 0.98$ and ≤ 64.38 meV/Å, indicating the high accuracy of the NNP, see SI note 2.

Table 1: Defect migration barriers (E_b) calculated using DFT and the NNPs for the NEB migration paths.

System	E_b^{DFT} (eV)	E_b^{NNP} (eV)
I_1^-	0.37	0.33
V_1^+	0.56	0.51
V_{MA}^0	0.70	0.72
V_{MA}^-	0.67	0.78
I_{MA}^+	0.70	0.67
I_{MA}^0	0.74	0.75

Results

Following training and validation, the NNPs are used to perform three independent 2 nanosecond (ns) long MD simulations at each temperature for five temperatures between 500 K and 600 K. The details of these production runs are given in the SI note 4. From these simulations, diffusion coefficients are extracted, providing the temperature-dependent diffusion behavior. As ion transport in MAPb_3 via interstitials or vacancies takes place through kick-out processes, tracer diffusion is not appropriate for characterizing transport. Instead we include all atoms or molecules of a particular species in calculating the diffusion coefficient, using the Einstein relation, which links the slope of the mean square displacement to time

$$D = \frac{1}{6} \lim_{t \rightarrow \infty} \frac{d}{dt} \left\langle \sum_{i=1}^N \|\mathbf{r}_i(t + t_0) - \mathbf{r}_i(t_0)\|^2 \right\rangle_{t_0}; \quad t > t_0 \quad (1)$$

where N is the number of atoms of a particular species in the simulation box, and \mathbf{r}_i are the atomic positions. Notwithstanding the fact that all ions participate in extracting the diffusion coefficient D , in the following we will still label them according to the defect, interstitial or vacancy, that instigates the diffusion.

The diffusion coefficients D extracted from the simulations are given in Figure 2. For iodide in-

terstitial I_1^- and vacancy V_1^+ , the diffusion coefficients are within a factor of five of one another within the given temperature range, with the interstitial being the more mobile of the two. Remarkably, also the diffusion coefficients of the neutral and positive MA interstitials I_{MA}^0 , I_{MA}^+ are within the same range. The MA vacancies V_{MA}^0 , V_{MA}^- are found to be immobile in the simulated temperature and time ranges.

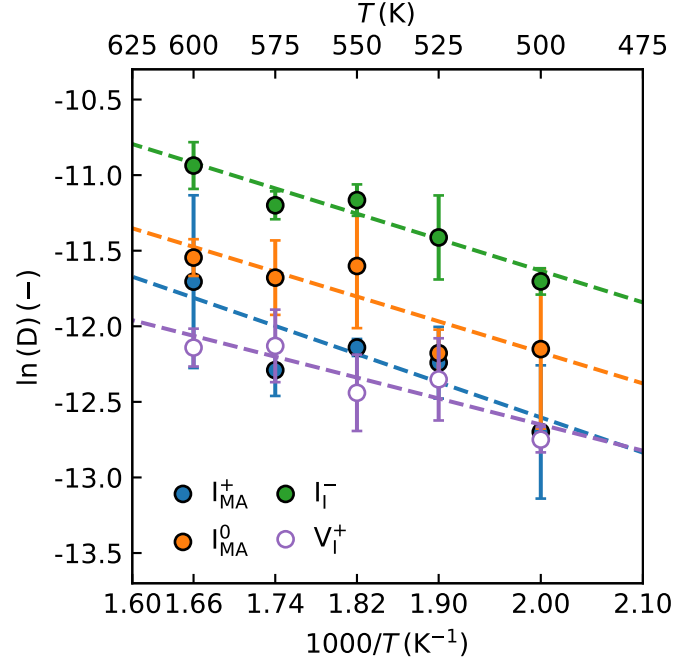


Figure 2: Temperature-dependent diffusion coefficients of iodide interstitial (I_1^-), iodide vacancy (V_1^+), neutral MA interstitial (I_{MA}^0), and positive MA interstitial (I_{MA}^+) defects in MAPb_3 . The dashed lines represent the fits to an Arrhenius expression, and the error bars represent the standard error in mean at each point.

For all defects the temperature dependence of the diffusion coefficient can be fitted to an Arrhenius relation

$$D = D_0 \exp\left(-\frac{E_a}{k_B T}\right) \quad (2)$$

where k_B is the Boltzmann constant, E_a the activation energy, and D_0 the pre-exponential factor. The fits are given in Figure 2, and the fit parameters along with the extrapolated diffusion coefficient at room temperature ($D_{300\text{K}}$) are presented in Table 2.

The activation energies and prefactors for in-

Table 2: Activation energies (E_a) and pre-exponential factors (D_0) extracted from the Arrhenius fits, and extrapolated diffusion constants (D_{300K}) at room temperature for iodide interstitial (I_1^-), iodide vacancy (V_1^+), neutral MA interstitial (I_{MA}^0), and positive MA interstitial (I_{MA}^+) in MAPbI₃.

System	E_a (eV)	D_0 ($\times 10^{-4}$ cm ² s ⁻¹)	D_{300K} ($\times 10^{-7}$ cm ² s ⁻¹)
I_1^-	0.18 ± 0.03	5.93 ± 3.97	5.61
V_1^+	0.15 ± 0.04	1.04 ± 0.92	3.19
I_{MA}^0	0.18 ± 0.06	3.16 ± 4.27	2.99
I_{MA}^+	0.20 ± 0.07	3.47 ± 5.12	1.51

terstitial I_1^- and vacancy, V_1^+ are quite close, and their extrapolated diffusion coefficients at 300 K are within a factor of two. The numbers are also quite close to those found for halide interstitials in CsPbI₃, CsPbBr₃ and CsPb(I_xBr_{1-x})₃,^{47,49} indicating that halide diffusion in 3D perovskites does not depend too much on the A cation in the lattice.

Diffusion coefficients for MA interstitials have similar prefactors as those for I defects, and only slightly higher activation energies, which demonstrates that MA interstitials are as mobile as I defects. In addition, the charge state of the MA interstitial does not seem to impact its migration behavior much. A neutral MA interstitial I_{MA}^0 creates one donor level very close to the conduction band edge,^{40,50} implying that at room or higher temperatures the MA interstitial will be ionized I_{MA}^+ . Indeed, a charge density analysis shows that for I_{MA}^0 the extra electron delocalizes over the whole lattice (SI note 5), such that it does not impact the motion of the MA interstitial much.

From the fact that MA vacancies are immobile during a 2 ns simulation at the highest temperature considered here (600 K), one can estimate a lower bound for their activation energy E_a . Assuming Arrhenius behavior with a prefactor similar to the other defects $D_0 \approx 10^{-4}$ cm²s⁻¹, gives an attempt frequency $\nu_0 \approx 0.5$ THz.⁴⁷ The number of migration events in 2 ns then drops below one for $E_a \approx 0.4$ eV.

To gain atomistic insights into the diffusion behaviour of these defects, trajectories are analyzed as defects migrate. Iodide defects migrate very similar to the way they do in CsPbI₃.⁴⁷ Vacancies V_1^+ move through a kick-out mechanism with a neighboring I atom rotating 90° around the Pb–I bond filling in the vacancy. The migration path for I_1^- interstitials consists of hopping moves of

an I atom from one Pb–II–Pb double bridge to a neighboring Pb–I–Pb bond to form a double bridge there.

The MA interstitial migrates through the concerted motion of three neighboring MA ions (Figure 3). The MA interstitial exists most frequently as two MA ions in one Pb–I cage with their C–N axes oriented approximately perpendicular to each other (Figure 3a). Migration is instigated by these two MA ions and a neighboring MA ion rotating such that their C–N axes align approximately parallel to each other (Figure 3b). Finally, the MA ion in the center migrates from one Pb–I cage to the neighboring one (Figure 3c).

Discussion

To place our results in context, we compare the calculated migration barriers (Table 2) with the wide range of experimentally reported activation energies (Table 3) for ion migration in MAPbI₃. Most experimental data gathered on ion migration in MAPbI₃ have been assigned to halide migration,⁶³ with reported activation energies from 0.10 to 0.68 eV, extracted with different measurement techniques, including conductivity/current measurements,^{16,19,22,23} capacitance/impedance measurements,^{24,28–31} photoluminescence,^{14,20,21} photocurrent relaxation,¹⁵ current response measurements,¹⁸ ionic current measurements,²⁵ and transient ion drift.²⁶ Some experiments also report results assigned to the diffusion of MA cations with barriers between 0.23 and 0.94 eV, from conductivity/current measurements,^{17,23} impedance measurements,^{27,28} deep-level transient spectroscopy,³⁰ and ionic current measurements.²⁵ Apart from technical issues and interpretational difficulties regarding the experi-

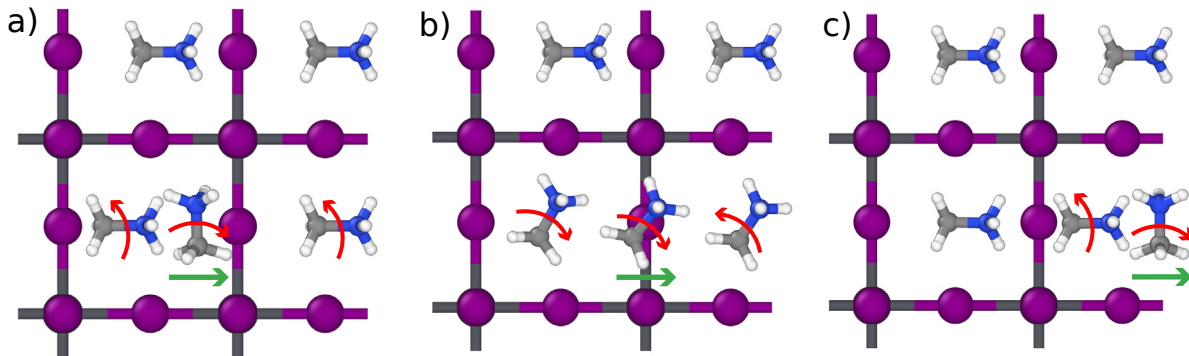


Figure 3: Schematic representation of the diffusion of the MA interstitial. The red arrows represent the rotation of the MA ion along the C–N axis, and the green arrows represent the migration paths.

mental data,^{63,64} it is clear that there is a considerable spread in these numbers.

Calculated activation barriers are typically based on NEB calculations, with numbers reported for the iodide vacancy of 0.08-0.58 eV, the iodide interstitial 0.08 eV, the MA vacancy 0.46-0.96 eV.^{15,34–39} The considerable spread in those numbers is associated with the difficulties of finding the lowest energy path for diffusion in a soft material such as MAPbI₃, where moreover the asymmetry of the MA cation may give rise to multiple competing paths.

Our MD simulations sample all these paths according to the appropriate thermal distribution, and yield a consistent set of activation energies in a narrow range of 0.15-0.20 eV, thereby supporting the lower values of the experimental spread. One should remark that in order to gather sufficient statistics regarding migration events, we have performed the simulations at elevated temperatures, $T \geq 500$ K, and assume that the Arrhenius expression for the diffusion coefficient, Eq. 2, holds for temperatures down to room temperature. This assumption might in principle be tested using rare-event sampling techniques, but that would involve a considerable computational effort outside the scope of the present paper.

As for the identification of the moving halide defect, from the simulations there is little difference in the mobility of the iodide vacancy or interstitial. Under equilibrium conditions the interstitial is the most favored point defect,^{40,50} but under non-equilibrium conditions the vacancy might of course occur.

As for the MA defect, there is a clear distinc-

tion between interstitial and vacancy, where the simulation predicts the MA vacancy to be immobile within the simulated temperature and time scales, whereas the MA interstitial has a mobility comparable to that of the iodide defects. The latter challenges the common assumption that MA migration is intrinsically slow due to its molecular nature. Our calculated migration barrier of 0.20 eV for I_{MA}^+ (Table 2) is in agreement with the values obtained experimentally by Reichert et al. (Table 3) using impedance spectroscopy (0.18 eV) and deep-level transient spectroscopy (0.23 eV).³⁰ Again, equilibrium conditions favor the formation of interstitials,^{40,50} with the MA vacancy only occurring under very iodine-rich conditions.

Some of the spread in experimental numbers might be explained by a difference in time and length scales caused by the inhomogeneity of the samples. These are typically multi-crystalline thin films, where diffusion in a crystalline grain will be different from that at grain boundaries/surfaces or between grains. As our simulations only consider bulk diffusion, this might suggest that the higher numbers observed in experiments refer to inter-grain diffusion.

Conclusions

In summary, we study the diffusion of iodide and MA interstitials and vacancies in MAPbI₃. We trained a neural network potential for the most stable charge states of these defects (I_I^- , I_{MA}^+ , V_I^+ , and V_{MA}^-), and separate neural network potentials for neutral MA interstitial (I_{MA}^0) and vacancy

Table 3: Experimentally reported activation energies for defect migration.

Technique	Activation energy (eV)	Migrating Species
Bulk conductivity ¹⁶	0.43	-
Conductivity ¹⁷	0.36	MA ⁺ ion
Current density ¹⁹	0.23-0.31	I _I ⁻
Conductivity ²²	0.08-0.14 and 0.47	-
Current density ²³	0.10 and 0.41	V _I ⁺ and V _{MA} ⁻
Ionic current ²⁵	0.28 and 0.94	V _I ⁺ and V _{MA} ⁻
Current response ¹⁸	0.10-0.18	V _I ⁺
Impedance spectroscopy ²⁷	0.58	MA ⁺ ion
Impedance spectroscopy ²⁸	0.55 and 0.68	V _I ⁺ and V _{MA} ⁻
Impedance spectroscopy ²⁹	0.13	halide ions
Impedance spectroscopy ³⁰	0.18	I _{MA} ⁺
Impedance spectroscopy ³¹	0.50	halide anions
Capacitive signature ²⁴	0.36	-
Deep-level transient spectroscopy ³⁰	0.23 and 0.14	I _{MA} ⁺ and I _I ⁻
Photoluminescence rise rates ¹⁴	0.27	halide ions
Photoluminescence rise rates ²⁰	0.14	Iodide defects
Photoluminescence rise rates ²¹	0.19	Iodide defects
Photocurrent relaxation ¹⁵	0.60-0.68	V _I ⁺
Transient ion-drift ²⁶	0.29 and 0.39-0.90	I ⁻ ion and MA ⁺ ion

(V_{MA}^0) using DFT calculations. Using these force fields, we performed MD simulations to study the migration behaviour of these defects.

We find that all defects besides MA vacancies are mobile with migration barriers in a narrow range of 0.15-0.20 eV, consistent with the lower end of experimentally reported activation energies. The migration rates of the MA interstitials are very similar to those of iodide point defects, despite MA interstitials being much bulkier than iodide defects. We attribute this finding to the concerted motion of three neighboring MA ions facilitating MA interstitial migration. In addition, our findings suggest that unlike iodide point defects, where the migration rates depend on the defect charge state, those of MA defects are not impacted by the charge state.

These findings provide a unified microscopic interpretation of ion migration in MAPbI₃ and help reconcile the wide range of activation energies reported experimentally. We show that low activation energies reflect intrinsic bulk diffusion dominated by iodide defects and MA interstitials, whereas higher activation energies reported experimentally likely reflect additional contributions,

such as inter-grain transport or formation of complex defects. Overall, our results revise the conventional picture of ionic transport in hybrid perovskites and highlight the importance of collective molecular motion in enabling fast ion migration.

Acknowledgement V.T. and S.T. acknowledge funding from Vidi (project no. VI.Vid.213.091) from the Dutch Research Council (NWO).

Data Availability

The training sets for the models used in this article are available in ref.⁶⁵

References

- (1) Shen, X. et al. Key Advancements and Emerging Trends of Perovskite Solar Cells in 2024–2025. *Nano-Micro Lett.* **2026**, *18*, 209.
- (2) Yi, C.; Luo, J.; Meloni, S.; Boziki, A.; Ashari-Astani, N.; Grätzel, C.; Zakeerud-

- din, S. M.; Röthlisberger, U.; Grätzel, M. Entropic stabilization of mixed A-cation ABX₃ metal halide perovskites for high performance perovskite solar cells. *Energy Environ. Sci.* **2016**, *9*, 656–662.
- (3) Bag, S.; Durstock, M. F. Large Perovskite Grain Growth in Low-Temperature Solution-Processed Planar p-i-n Solar Cells by Sodium Addition. *ACS Appl. Mater. Interfaces* **2016**, *8*, 5053–5057.
- (4) Ball, J. M.; Petrozza, A. Defects in perovskite-halides and their effects in solar cells. *Nat. Energy* **2016**, *1*, 16149.
- (5) Wang, F.; Bai, S.; Tress, W.; Hagfeldt, A.; Gao, F. Defects engineering for high-performance perovskite solar cells. *npj Flex. Electron.* **2018**, *2*, 22.
- (6) Thiesbrummel, J. et al. Ion-induced field screening as a dominant factor in perovskite solar cell operational stability. *Nat. Energy* **2024**, *9*, 664–676.
- (7) Apergi, S.; Koch, C.; Brocks, G.; Olthof, S.; Tao, S. Decomposition of Organic Perovskite Precursors on MoO₃: Role of Halogen and Surface Defects. *ACS Appl. Mater. Interfaces* **2022**, *14*, 34208–34219.
- (8) Apergi, S.; Brocks, G.; Tao, S.; Olthof, S. Probing the Reactivity of ZnO with Perovskite Precursors. *ACS Appl. Mater. Interfaces* **2024**, *16*, 14984–14994.
- (9) Semerci, A. et al. The Role of Fluorine-Functionalized Organic Spacers for Defect Passivation and Low-Dimensional Phase Formation in 3D MAPbI₃ Perovskite Solar Cells. *Adv. Funct. Mater.* **2025**, *35*, 2423109.
- (10) Maschwitz, T. et al. How crystallization additives govern halide perovskite grain growth. *Nat. Commun.* **2025**, *16*, 9894.
- (11) Xue, H.; Vicent-Luna, J. M.; Tao, S.; Brocks, G. Compound Defects in Halide Perovskites: A First-Principles Study of CsPbI₃. *J. Phys. Chem. C* **2023**, *127*, 1189–1197.
- (12) Clark, C. P.; Mann, J. E.; Bangsund, J. S.; Hsu, W.-J.; Aydil, E. S.; Holmes, R. J. Formation of Stable Metal Halide Perovskite/Perovskite Heterojunctions. *ACS Energy Lett.* **2020**, *5*, 3443–3451.
- (13) Thiesbrummel, J.; Milić, J. V.; Deibel, C.; Garnett, E. C.; Tao, S.; Kirchartz, T.; Guerrero, A.; Cameron, P.; Tress, W.; Saiful Islam, M.; Ehrler, B. Ion migration in perovskite solar cells. *Nat. Rev. Chem.* **2026**, *10*, 179–195.
- (14) Hoke, E. T.; Slotcavage, D. J.; Dohner, E. R.; Bowering, A. R.; Karunadasa, H. I.; McGehee, M. D. Reversible photo-induced trap formation in mixed-halide hybrid perovskites for photovoltaics. *Chem. Sci.* **2014**, *6*, 613–617.
- (15) Eames, C.; Frost, J. M.; Barnes, P. R. F.; O'Regan, B. C.; Walsh, A.; Islam, M. S. Ionic transport in hybrid lead iodide perovskite solar cells. *Nat. Commun.* **2015**, *6*, 7497, Publisher: Nature Publishing Group.
- (16) Yang, T.-Y.; Gregori, G.; Pellet, N.; Grätzel, M.; Maier, J. The Significance of Ion Conduction in a Hybrid Organic–Inorganic Lead-Iodide-Based Perovskite Photosensitizer. *Angew. Chem.* **2015**, *54*, 7905–7910.
- (17) Yuan, Y.; Chae, J.; Shao, Y.; Wang, Q.; Xiao, Z.; Centrone, A.; Huang, J. Photovoltaic Switching Mechanism in Lateral Structure Hybrid Perovskite Solar Cells. *Adv. Energy Mater.* **2015**, *5*, 1500615.
- (18) Yu, H.; Lu, H.; Xie, F.; Zhou, S.; Zhao, N. Native Defect-Induced Hysteresis Behavior in Organolead Iodide Perovskite Solar Cells. *Adv. Funct. Mater.* **2016**, *26*, 1411–1419.
- (19) Li, C.; Tscheuschner, S.; Paulus, F.; Hopkinson, P. E.; Kießling, J.; Köhler, A.; Vaynzof, Y.; Huettner, S. Iodine Migration and its Effect on Hysteresis in Perovskite Solar Cells. *Adv. Mater.* **2016**, *28*, 2446–2454.
- (20) Mosconi, E.; Meggiolaro, D.; Snaith, H. J.; Stranks, S. D.; De Angelis, F. Light-induced

- annihilation of Frenkel defects in organolead halide perovskites. *Energy Environ. Sci.* **2016**, *9*, 3180–3187.
- (21) deQuilettes, D. W.; Zhang, W.; Burlakov, V. M.; Graham, D. J.; Leijtens, T.; Osherov, A.; Bulović, V.; Snaith, H. J.; Ginger, D. S.; Stranks, S. D. Photo-induced halide redistribution in organic–inorganic perovskite films. *Nat. Commun.* **2016**, *7*, 11683.
- (22) Xing, J.; Wang, Q.; Dong, Q.; Yuan, Y.; Fang, Y.; Huang, J. Ultrafast ion migration in hybrid perovskite polycrystalline thin films under light and suppression in single crystals. *Phys. Chem. Chem. Phys.* **2016**, *18*, 30484–30490.
- (23) Game, O. S.; Buchsbaum, G. J.; Zhou, Y.; Padture, N. P.; Kingon, A. I. Ions Matter: Description of the Anomalous Electronic Behavior in Methylammonium Lead Halide Perovskite Devices. *Adv. Funct. Mater.* **2017**, *27*, 1606584.
- (24) Awni, R. A.; Song, Z.; Chen, C.; Li, C.; Wang, C.; Razzoqi, M. A.; Chen, L.; Wang, X.; Ellingson, R. J.; Li, J. V.; Yan, Y. Influence of Charge Transport Layers on Capacitance Measured in Halide Perovskite Solar Cells. *Joule* **2020**, *4*, 644–657.
- (25) Schmidt, M. C.; Alvarez, A. O.; Pallotta, R.; Seid, B. A.; de Boer, J. J.; Thiesbrummel, J.; Lang, F.; Grancini, G.; Ehrler, B. Quantification of Mobile Ions in Perovskite Solar Cells with Thermally Activated Ion Current Measurements. *ACS Energy Lett.* **2026**, *11*, 409–418.
- (26) Futscher, M. H.; Lee, J. M.; McGovern, L.; Muscarella, L. A.; Wang, T.; Haider, M. I.; Fakhruddin, A.; Schmidt-Mende, L.; Ehrler, B. Quantification of ion migration in CH₃NH₃PbI₃ perovskite solar cells by transient capacitance measurements. *Mater. Horiz.* **2019**, *6*, 1497–1503.
- (27) Bag, M.; Renna, L. A.; Adhikari, R. Y.; Karak, S.; Liu, F.; Lahti, P. M.; Russell, T. P.; Tuominen, M. T.; Venkataraman, D. Kinetics of Ion Transport in Perovskite Active Layers and Its Implications for Active Layer Stability. *J. Am. Chem. Soc.* **2015**, *137*, 13130–13137.
- (28) Pockett, A.; Eperon, G. E.; Sakai, N.; Snaith, H. J.; Peter, L. M.; Cameron, P. J. Microseconds, milliseconds and seconds: deconvoluting the dynamic behaviour of planar perovskite solar cells. *Phys. Chem. Chem. Phys.* **2017**, *19*, 5959–5970.
- (29) Futscher, M. H.; Gangishetty, M. K.; Congreve, D. N.; Ehrler, B. Quantifying mobile ions and electronic defects in perovskite-based devices with temperature-dependent capacitance measurements: Frequency vs time domain. *J. Chem. Phys.* **2020**, *152*, 044202.
- (30) Reichert, S.; An, Q.; Woo, Y.-W.; Walsh, A.; Vaynzof, Y.; Deibel, C. Probing the ionic defect landscape in halide perovskite solar cells. *Nat. Commun.* **2020**, *11*, 6098.
- (31) McGovern, L.; Koschany, I.; Grimaldi, G.; Muscarella, L. A.; Ehrler, B. Grain Size Influences Activation Energy and Migration Pathways in MAPbBr₃ Perovskite Solar Cells. *J. Phys. Chem. Lett.* **2021**, *12*, 2423–2428.
- (32) Bokdam, M.; Lahnsteiner, J.; Ramberger, B.; Schäfer, T.; Kresse, G. Assessing Density Functionals Using Many Body Theory for Hybrid Perovskites. *Phys. Rev. Lett.* **2017**, *119*, 145501.
- (33) Lahnsteiner, J.; Kresse, G.; Heinen, J.; Bokdam, M. Finite-temperature structure of the MAPbI₃ perovskite: Comparing density functional approximations and force fields to experiment. *Phys. Rev. Mater.* **2018**, *2*, 073604.
- (34) Haruyama, J.; Sodeyama, K.; Han, L.; Tateyama, Y. First-Principles Study of Ion Diffusion in Perovskite Solar Cell Sensitizers. *J. Am. Chem. Soc.* **2015**, *137*, 10048–10051.

- (35) Azpiroz, J. M.; Mosconi, E.; Bisquert, J.; De Angelis, F. Defect migration in methylammonium lead iodide and its role in perovskite solar cell operation. *Energy Environ. Sci.* **2015**, *8*, 2118–2127.
- (36) Pazoki, M.; Wolf, M.; Edvinsson, T.; Kullgren, J. Vacancy dipole interactions and the correlation with monovalent cation dependent ion movement in lead halide perovskite solar cell materials. *Nano Energy* **2017**, *38*, 537–543.
- (37) Ferdani, D. W.; Pering, S. R.; Ghosh, D.; Kubiak, P.; Walker, A. B.; Lewis, S. E.; Johnson, A. L.; Baker, P. J.; Islam, M. S.; Cameron, P. J. Partial cation substitution reduces iodide ion transport in lead iodide perovskite solar cells. *Energy Environ. Sci.* **2019**, *12*, 2264–2272.
- (38) Woo, Y. W.; Jung, Y.-K.; Kim, G. Y.; Kim, S.; Walsh, A. Factors influencing halide vacancy transport in perovskite solar cells. *Discov. Mater.* **2022**, *2*, 8.
- (39) Zhao, C.; Cazorla, C.; Zhang, X.; Huang, H.; Zhao, X.; Li, D.; Shi, J.; Zhao, Q.; Ma, W.; Yuan, J. Fast Organic Cation Exchange in Colloidal Perovskite Quantum Dots toward Functional Optoelectronic Applications. *J. Am. Chem. Soc.* **2024**, *146*, 4913–4921.
- (40) Xue, H.; Brocks, G.; Tao, S. First-principles calculations of defects in metal halide perovskites: A performance comparison of density functionals. *Phys. Rev. Mater.* **2021**, *5*, 125408.
- (41) Xue, H.; Brocks, G.; Tao, S. Intrinsic defects in primary halide perovskites: A first-principles study of the thermodynamic trends. *Phys. Rev. Mater.* **2022**, *6*, 055402.
- (42) Delugas, P.; Caddeo, C.; Filippetti, A.; Mattoni, A. Thermally Activated Point Defect Diffusion in Methylammonium Lead Trihalide: Anisotropic and Ultrahigh Mobility of Iodine. *J. Phys. Chem. Lett.* **2016**, *7*, 2356–2361.
- (43) Balestra, S. R. G.; Vicent-Luna, J. M.; Calero, S.; Tao, S.; Anta, J. A. Efficient modelling of ion structure and dynamics in inorganic metal halide perovskites. *J. Mater. Chem. A* **2020**, *8*, 11824–11836.
- (44) Behler, J. Four generations of high-dimensional neural network potentials. *Chem. Rev.* **2021**, *121*, 10037–10072.
- (45) Unke, O. T.; Chmiela, S.; Sauceda, H. E.; Gastegger, M.; Poltavsky, I.; Schütt, K. T.; Tkatchenko, A.; Müller, K.-R. Machine Learning Force Fields. *Chem. Rev.* **2021**, *121*, 10142–10186.
- (46) Wu, S.; Yang, X.; Zhao, X.; Li, Z.; Lu, M.; Xie, X.; Yan, J. Applications and Advances in Machine Learning Force Fields. *J. Chem. Inf. Model.* **2023**, *63*, 6972–6985.
- (47) Tyagi, V.; Pols, M.; Brocks, G.; Tao, S. Tracing Ion Migration in Halide Perovskites with Machine Learned Force Fields. *J. Phys. Chem. Lett.* **2025**, *16*, 5153–5159.
- (48) Mosquera-Lois, I.; Klarbring, J.; Walsh, A. Point defect formation at finite temperatures with machine learning force fields. *Chem. Sci.* **2025**, *16*, 8878–8888.
- (49) Tyagi, V.; Pols, M.; Brocks, G.; Tao, S. Halide Diffusion in Mixed-Halide Perovskites and Heterojunctions. *Chem. Mater.* **2026**,
- (50) Meggiolaro, D.; De Angelis, F. First-Principles Modeling of Defects in Lead Halide Perovskites: Best Practices and Open Issues. *ACS Energy Lett.* **2018**, *3*, 2206–2222.
- (51) Batzner, S.; Musaelian, A.; Sun, L.; Geiger, M.; Mailoa, J. P.; Kornbluth, M.; Molinari, N.; Smidt, T. E.; Kozinsky, B. E(3)-equivariant graph neural networks for data-efficient and accurate interatomic potentials. *Nat. Comm.* **2022**, *13*, 2453.
- (52) Musaelian, A.; Batzner, S.; Johansson, A.; Sun, L.; Owen, C. J.; Kornbluth, M.; Kozinsky, B. Learning local equivariant representations for large-scale atomistic dynamics. *Nat. Comm.* **2023**, *14*, 579.

- (53) Kresse, G.; Furthmüller, J. Efficient iterative schemes for ab initio total-energy calculations using a plane-wave basis set. *Phys. Rev. B* **1996**, *54*, 11169–11186.
- (54) Jinnouchi, R.; Karsai, F.; Kresse, G. On-the-fly machine learning force field generation: Application to melting points. *Phys. Rev. B* **2019**, *100*, 014105.
- (55) Jinnouchi, R.; Lahnsteiner, J.; Karsai, F.; Kresse, G.; Bokdam, M. Phase Transitions of Hybrid Perovskites Simulated by Machine-Learning Force Fields Trained on the Fly with Bayesian Inference. *Phys. Rev. Lett.* **2019**, *122*, 225701.
- (56) Bartók, A. P.; Payne, M. C.; Kondor, R.; Csányi, G. Gaussian Approximation Potentials: The Accuracy of Quantum Mechanics, without the Electrons. *Phys. Rev. Lett.* **2010**, *104*, 136403.
- (57) Bartók, A. P.; Kondor, R.; Csányi, G. On representing chemical environments. *Phys. Rev. B* **2013**, *87*, 184115.
- (58) Sun, J.; Ruzsinszky, A.; Perdew, J. P. Strongly Constrained and Appropriately Normed Semilocal Density Functional. *Phys. Rev. Lett.* **2015**, *115*, 036402.
- (59) Sabatini, R.; Gorni, T.; de Gironcoli, S. Non-local van der Waals density functional made simple and efficient. *Phys. Rev. B* **2013**, *87*, 041108.
- (60) Motti, S. G.; Meggiolaro, D.; Barker, A. J.; Mosconi, E.; Perini, C. A. R.; Ball, J. M.; Gandini, M.; Kim, M.; De Angelis, F.; Petrozza, A. Controlling competing photochemical reactions stabilizes perovskite solar cells. *Nat. Photonics* **2019**, *13*, 532–539.
- (61) Ni, Z.; Jiao, H.; Fei, C.; Gu, H.; Xu, S.; Yu, Z.; Yang, G.; Deng, Y.; Jiang, Q.; Liu, Y.; Yan, Y.; Huang, J. Evolution of defects during the degradation of metal halide perovskite solar cells under reverse bias and illumination. *Nat. Energy* **2022**, *7*, 65–73.
- (62) Henkelman, G.; Uberuaga, B. P.; Jónsson, H. A climbing image nudged elastic band method for finding saddle points and minimum energy paths. *J. Chem. Phys.* **2000**, *113*, 9901–9904.
- (63) Yantara, N.; Mathews, N. Toolsets for assessing ionic migration in halide perovskites. *Joule* **2024**, *8*, 1239–1273.
- (64) Schmidt, M. C.; Alvarez, A. O.; de Boer, J. J.; van de Ven, L. J.; Ehrler, B. Consistent Interpretation of Time- and Frequency-Domain Traces of Ion Migration in Perovskite Semiconductors. *ACS Energy Lett.* **2024**, *9*, 5850–5858.
- (65) Tyagi, V. Training sets for A unified microscopic picture of cation and anion migration in MAPbI₃. 2026; <https://doi.org/10.5281/zenodo.20052556>.

Supporting Information:

**A unified microscopic picture of cation and anion
migration in MAPbI₃**

Viren Tyagi,[†] Geert Brocks,^{†,‡} and Shuxia Tao^{*,†}

[†]*Department of Applied Physics and Science Education, Eindhoven University of Technology,
5600 MB, Eindhoven, The Netherlands*

[‡]*Computational Chemical Physics, Faculty of Science and Technology and MESA+ Institute for
Nanotechnology, University of Twente, 7500 AE, Enschede, The Netherlands*

E-mail: s.x.tao@tue.nl

Contents

1	Model training	S3
2	Model validation	S6
3	MAPbI₃ phase transition	S10
4	Production runs and diffusion coefficients	S13
5	Charge density analysis	S16
	References	S17

1 Model training

Training structures are sampled from three constant temperature MD runs using the on-the-fly learning procedure as implemented in VASP,¹⁻⁵ for both neutral and positively charged methylammonium interstitial (I_{MA}^0 and I_{MA}^+), neutral and negatively charged methylammonium vacancy (V_{MA}^0 and V_{MA}^-), and negatively charged iodide interstitial (I_I^-) and positively charged iodide vacancy (V_I^+). These runs are performed for 105 ps with an MD timestep of 3 fs and the mass of H increased to 4 amu, using $2 \times 2 \times 2$ cubic supercells of $MAPbI_3$ (96 atoms) with one MA or I point defect in them. Three such runs are performed for each system at temperatures between 500 K and 750 K (Table S1) in NpT ensembles at 10^5 Pa pressure. To maintain constant temperature and pressure, Parinello-Rahman dynamics^{6,7} is used with friction coefficients set to 3 ps^{-1} for all atomic species and lattice degrees of freedom.

Table S1: The number of structures (n) in the training set and temperatures at which the training runs are performed for different defect systems.

System	n	Step 1	Step 2	Step 3
I_{MA}^0	1485	600 K	700 K	500 K
I_{MA}^+	1596	700 K	700 K	500 K
V_{MA}^0	1339	600 K	700 K	500 K
V_{MA}^-	1328	600 K	700 K	500 K
I_I^-	1818	600 K	750 K	750 K
V_I^+	1501	600 K	750 K	750 K

The total number of structures sampled for all systems is given in Table S1. DFT single-point calculations are performed on all these structures in VASP. The projector-augmented wave (PAW)⁸ technique is used to model electron-ion interactions, with the outermost electrons of I ($5s^25p^5$), Pb ($6s^26p^2$), H ($1s^1$), C ($2s^22p^2$), and N ($2s^22p^3$) treated as valence electrons, and applying the standard VASP PAW potentials. The electronic interactions are modeled using the SCAN+rVV10 functional,^{9,10} as it has been shown to reliably describe the dynamics of the MA ion and defect formation energies.¹¹⁻¹³ An energy convergence criterion of 10^{-6} eV is used, along with a $2 \times 2 \times 2$ Monkhorst-Pack k -point grid¹⁴ and a kinetic energy cutoff of 500 eV.

Three different Allegro models^{15,16} are trained, one for all charged defects (I_{MA}^+ , V_{MA}^- , I_I^- , and

V_I^+), one for I_{MA}^0 , and one for V_{MA}^0 . The defects have these charge states when the Fermi level is well inside the band gap,¹³ and a single force field should be able to capture this. The neutral I_{MA}^0 (V_{MA}^0) can only be found when the Fermi energy is very close or in the conduction (valence) band, and separate force fields have to be constructed to describe these situations.

All of these models are trained using a radial cutoff of 6.5 Å with interatomic distances projected onto a radial basis using trainable Bessel functions, and 2 tensor product layers. 32 ordered-pair tensor features are used, expanded using spherical harmonics with a maximum angular quantum number (L_{\max}) of 2, while preserving full $O(3)$ symmetry. The 2-body latent multilayer perceptron (MLP) had the dimensions [128, 256, 512, 1024] and SiLU nonlinearity, and the latent MLP had the dimensions [1024, 1024, 1024] also with SiLU nonlinearity. To predict the pair energies, the final MLP has dimensions [128] without nonlinearity.

For all three models, the training and the validation sets are divided into 80% and 20% of the total number of structures (Table S2), respectively, which are shuffled at each epoch during training. The training is performed using the total energy of the system, forces acting on the atoms, and stress tensors. The per-atom MSE loss function is used, with the weight set to 1 for both energy and forces. The Adam optimizer in PyTorch is used with the default parameters $\beta_1 = 0.9$, $\beta_2 = 0.99$, and $\epsilon = 10^{-8}$. The learning rate of 0.001 and the batch size of 5 are used. The number of epochs the training of each model ran for is given in Table S2.

The root mean squared error (RMSE) in energy and forces during training and validation is given in Figure S1. The total number of epochs, and training and validation errors in energy and forces for the final model are given in Table S2.

Table S2: The total number of structures in the training and validation sets, number of epochs, training and validation errors in energy and forces for all models.

Model	n	epochs	$F_{\text{RMSE}}(\text{meV}/\text{\AA})$		$E_{\text{RMSE}}(\text{meV}/\text{atom})$	
			Training	Validation	Training	Validation
charged defects	6243	970	6.5	17.9	105	105
I_{MA}^0	1485	850	5.8	24.1	43	46.6
V_{MA}^0	1339	954	5.2	20.9	34.9	37.8

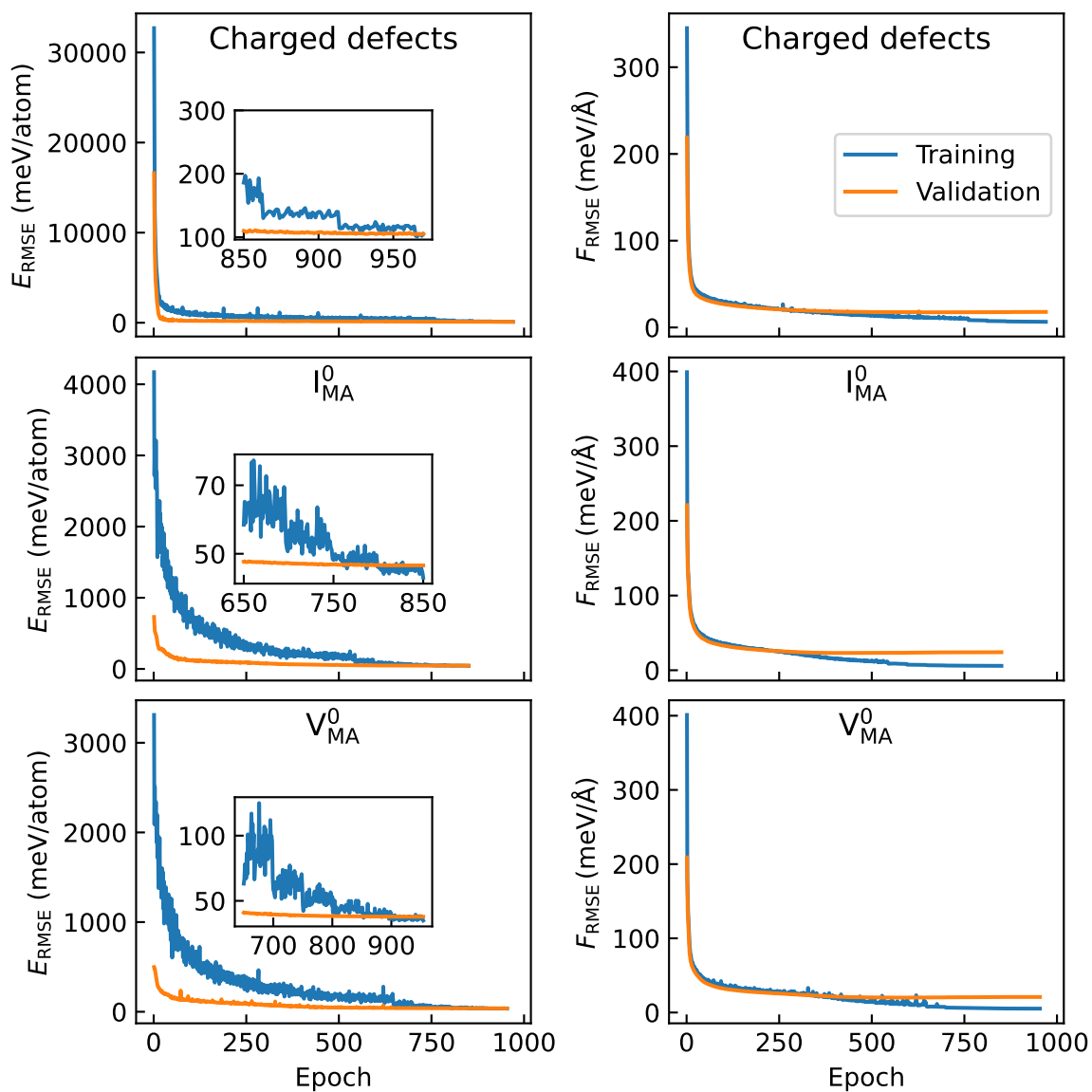


Figure S1: Root mean squared errors in energy (E_{RMSE}) and forces (F_{RMSE}) during model training and model validation of all models.

2 Model validation

To check the accuracy of the model in predicting forces, at least 10 structures are sampled from 0.5 ns MD runs at 600 K performed using $6 \times 6 \times 6$ cubic supercells of MAPbI_3 (2592 atoms) with one MA or I point defect, and forces calculated using DFT are compared with forces calculated using the NNP for these structures. The forces categorized according to the atomic species acting on all atoms, with the corresponding R^2 values and mean absolute errors (MAE) for the charged defects are given in Figure S2, and for neutral defects are given in Figure S3. From these comparisons, we note that the $R^2 = 0.99$ and $\text{MAE} \leq 29.83 \text{ meV}/\text{\AA}$ for all systems. Considering that the forces acting on these atoms are of the order of $1 \text{ eV}/\text{\AA}$, the NNPs are highly accurate in calculating forces acting on all atoms.

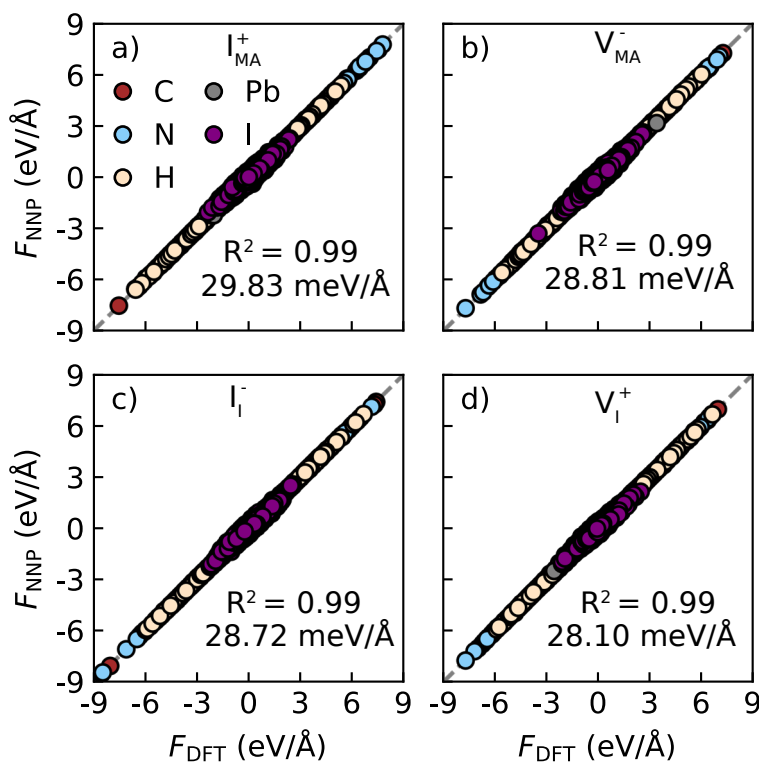


Figure S2: Comparison between forces acting on all atoms calculated by the charged defects NNP with forces calculated using DFT for $6 \times 6 \times 6$ cubic supercell of MAPbI_3 with one MA interstitial (a), one MA vacancy (b), one I interstitial (c), or one I vacancy, along with corresponding R^2 values and mean absolute errors (MAE).

Forces acting on the atoms close to the defect are also compared. MA defect environments

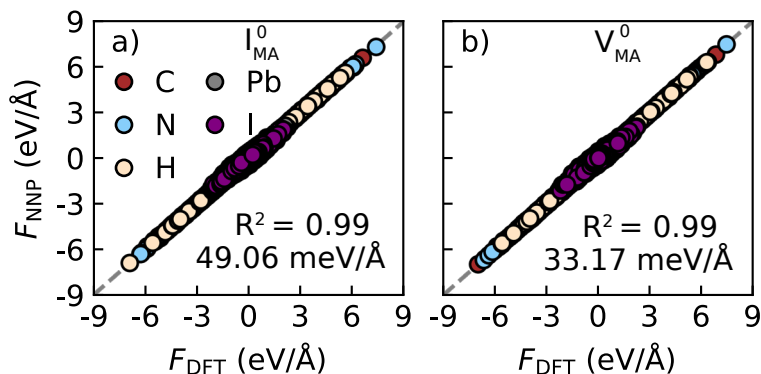


Figure S3: Comparison between forces acting on all atoms calculated by the neutral MA interstitial NNP (a) and neutral MA vacancy NNP (b) with forces calculated using DFT for $6 \times 6 \times 6$ cubic supercell of MAPbI_3 with one MA point defect, along with corresponding R^2 values and mean absolute errors (MAE).

are identified by counting the MA neighbors of Pb, as illustrated in Figure S4. For the MA interstitial (Figure S4a) the environment consists of Pb atoms with 9 MA neighbors, and for a MA vacancy (Figure S4b) the environment consists of Pb atoms with 7 MA neighbors. The I point defect environments are identified using the same procedure described in ref.¹⁷ These comparisons are given in Figure S5 for charged defects, and in Figure S6 for neutral defects. From these comparisons, we conclude that the NNPs also calculate forces acting on atoms in the defect environment with high accuracy, with the $R^2 \geq 0.96$ and $\text{MAE} \leq 64.38 \text{ meV}/\text{\AA}$ for all systems.

Along with the forces, the energies calculated with the NNPs are also compared with those calculated using DFT for paths constructed using the climbing image nudged elastic band (CI-NEB) method.¹⁸ These paths are constructed using $2 \times 2 \times 1$ supercell of MAPbI_3 (16 units) with one MA or I point defect. Three intermediate images, connected by springs with spring constants $5 \text{ eV}/\text{\AA}^2$, are optimized using the same DFT parameters as in Section 1, and a $2 \times 2 \times 3$ Monkhorst-Pack k -grid.

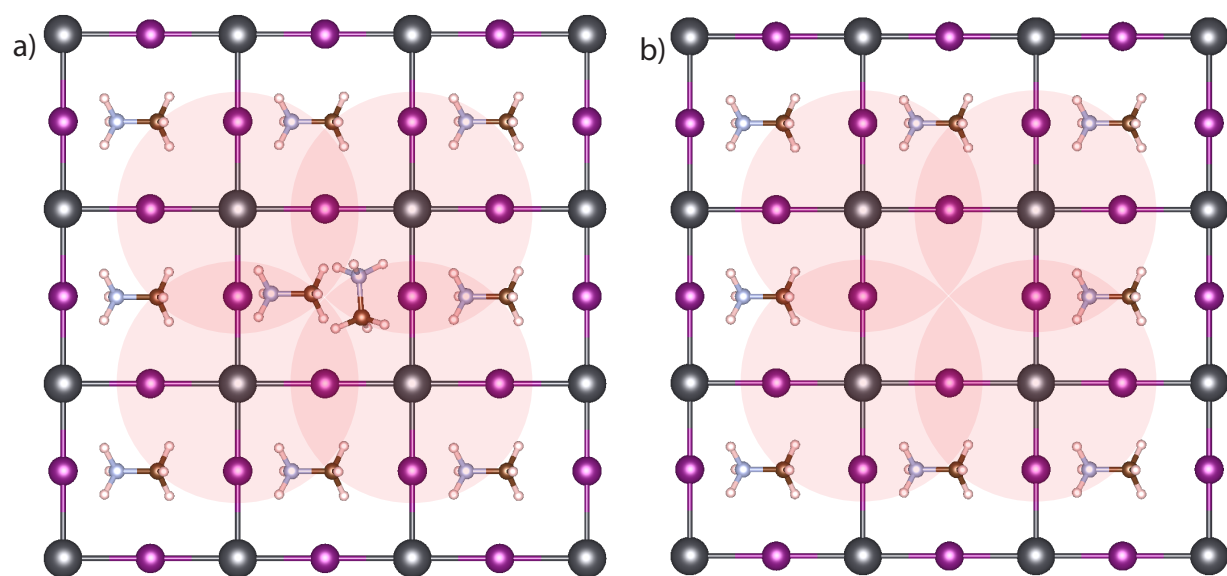


Figure S4: Illustration of how atoms close to the MA interstitial (a) and MA vacancy (b) are identified for model validation. Here, the red circles indicate the area used for selecting defect environment atoms.

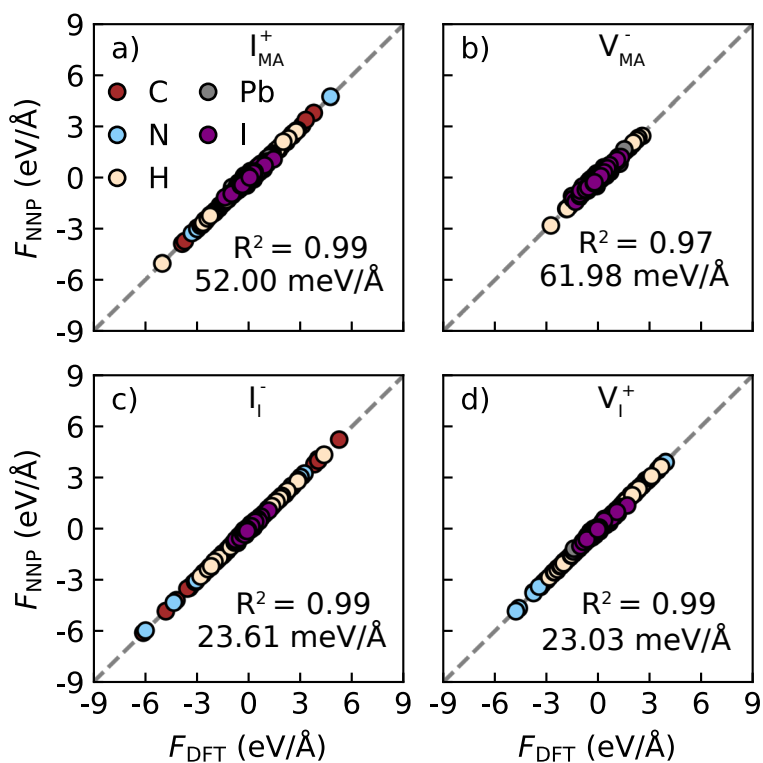


Figure S5: Comparison between forces acting on atoms in defect environment calculated by the charged defects NNP with forces calculated using DFT for a $6 \times 6 \times 6$ cubic supercell of MAPbI_3 with one MA interstitial (a), one MA vacancy (b), one I interstitial (c), or one I vacancy, along with corresponding R^2 values and mean absolute errors (MAE).

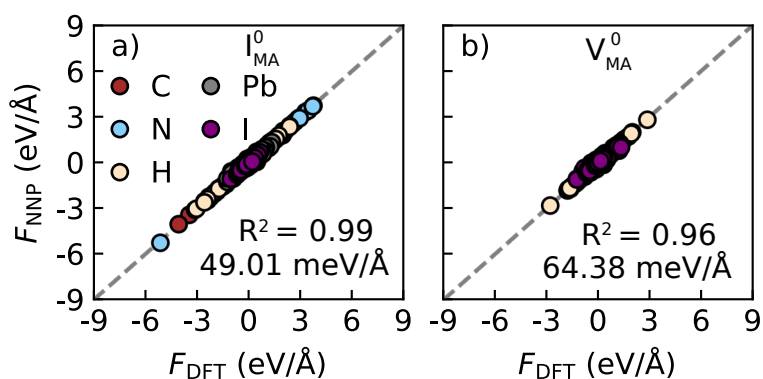


Figure S6: Comparison between forces acting on atoms in defect environment calculated by the neutral MA interstitial NNP (a) and neutral MA vacancy NNP (b) with forces calculated using DFT for $6 \times 6 \times 6$ cubic supercell of MAPbI_3 with one MA point defect, along with corresponding R^2 values and mean absolute errors (MAE).

3 MAPbI₃ phase transition

To test the method further and to extract the temperature dependence of the volume, a separate NNP is constructed to describe pristine MAPbI₃. Training structures are sampled from four constant temperature MD runs using the on-the-fly learning procedure as implemented in VASP. These runs are performed for 105 ps with an MD timestep of 3 fs and the mass of H increased to 4 amu using $2 \times 2 \times 2$ pseudo-cubic supercells of MAPbI₃ in all three perovskite phases. The first run is performed in the cubic phase at 450 K, followed by two runs in the tetragonal phase at 250 K and 150 K, and finally one run in the orthorhombic phase at 150 K. All these runs are performed in an NpT ensemble with Parinello-Rahman dynamics with friction coefficients set to 3 ps^{-1} for all atomic species and lattice degrees of freedom.

A total of 1132 structures are sampled, and DFT single-point calculations are performed on all these structures using the same DFT parameters as in SI note 1 to generate the final training and validation sets.

An Allegro model is trained using the same model parameters as in SI note 1, with the training and validation sets consisting of 905 and 227 structures, respectively, and the training ran for 1134 epochs. The RMSE in energy and forces during model training and model validation are given in Figure S7. The final model has the training errors of 24.5 meV/atom in energy and 5.04 meV/Å in forces, and validation errors of 24.23 meV/atom in energy and 11.7 meV/Å in forces.

The accuracy and transferability of this model are validated by performing heating runs from 100 K to 400 K for 0.6 ns using a time step of 1 fs on $3 \times 3 \times 2$ orthorhombic supercells (72 units) of MAPbI₃. The window-averaged pseudo-cubic lattice vectors with the window lengths 5 ps from this run are given in Figure S8. The overall phase diagram closely resembles that observed in experiments.¹⁹

This NNP is used to perform constant temperature MD runs in an NpT ensemble using $6 \times 6 \times 6$ cubic supercells (216 units) of MAPbI₃ at different temperatures between 300 K and 450 K with steps of 50 K to obtain equilibrated lattice constants. These values are fitted

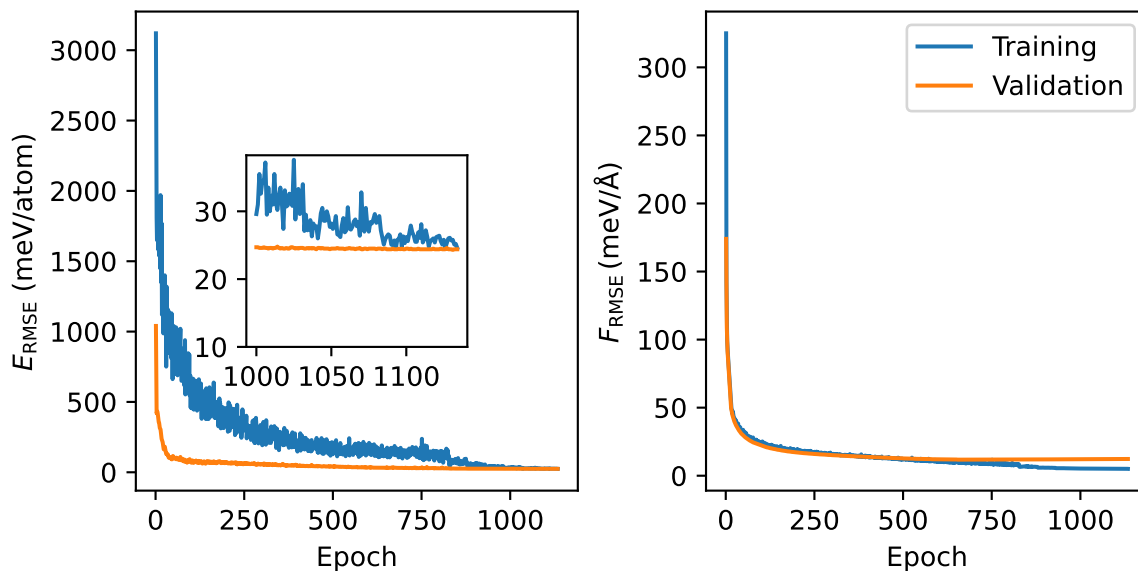


Figure S7: Root mean squared errors in energy (E_{RMSE}) and forces (F_{RMSE}) during model training and model validation of the MAPbI_3 phase transition model.

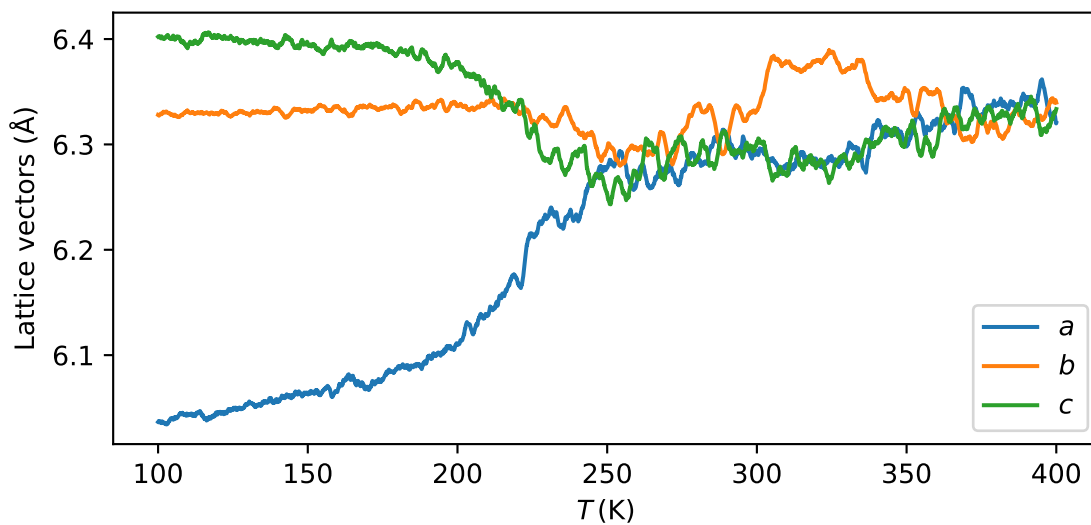


Figure S8: Pseudo-cubic unit cell lattice vectors of MAPbI_3 as functions of temperature in the heating MD runs performed using the phase transition NNP.

using linear least-squares regression (Figure S9) and extrapolated to obtain equilibrated volumes between 500 K and 600 K.

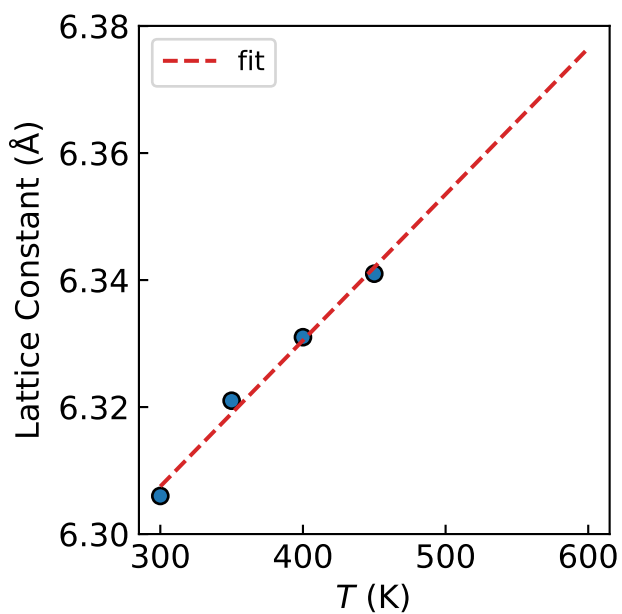


Figure S9: The lattice constant of cubic MAPbI_3 as a function of temperature extracted using the phase transition NNP. The blue points represent calculated values, and the dotted red line represents the fit.

4 Production runs and diffusion coefficients

2 ns long MD runs are performed at different temperatures between 500 K and 600 K using $6 \times 6 \times 6$ supercells (216 units of MAPbI_3) with one MA or I point defect in LAMMPS.²⁰ The lattice constants are obtained using the procedure described in SI note 3, and are given in Table S3.

Table S3: Lattice constants of MAPbI_3 unit cell at different temperatures in cubic phase.

Temperature (K)	Lattice constants (Å)
500	6.354
525	6.359
550	6.365
575	6.371
600	6.377

The structures are first equilibrated to the target temperature for 100 ps with timesteps of 1 fs in an NVT ensemble using a Langevin thermostat with the relaxation time set to 0.33 ps. Following equilibration, 2 ns long production runs with timesteps of 1 fs are performed in an NVT ensemble using a Nose-Hoover thermostat with the relaxation time set to 0.1 ps. To ensure proper sampling of diffusion coefficients, 5 runs are performed at each temperature. To quantify the migration behavior of the defects, the mean squared displacement (MSD) is plotted over time for each atomic species using the MDAnalysis Python library.^{21,22} The MSD plots for I_{MA}^+ and I_1^- are given in Figure S10 and Figure S11, respectively. The MSD is calculated using

$$\text{MSD}(r_d) = \left\langle \frac{1}{N} \sum_{i=1}^N |r_d - r_d(t_0)|^2 \right\rangle_{t_0}, \quad (\text{S1})$$

where N is the number of atoms of a particular atomic species, and r_d are their coordinates in d dimensions (3 for our systems). The Diffusion coefficient D is calculated using

$$D = \frac{N}{2d} \lim_{t \rightarrow \infty} \frac{d}{dt} \text{MSD}(r_d), \quad (\text{S2})$$

which is proportional to the slope of the MSD curve, where the factor N ensures that the diffusion

coefficient is defect concentration independent. The diffusion coefficient of the MA molecule is calculated as the average of the diffusion coefficients of C,N, and H (Figure S10).

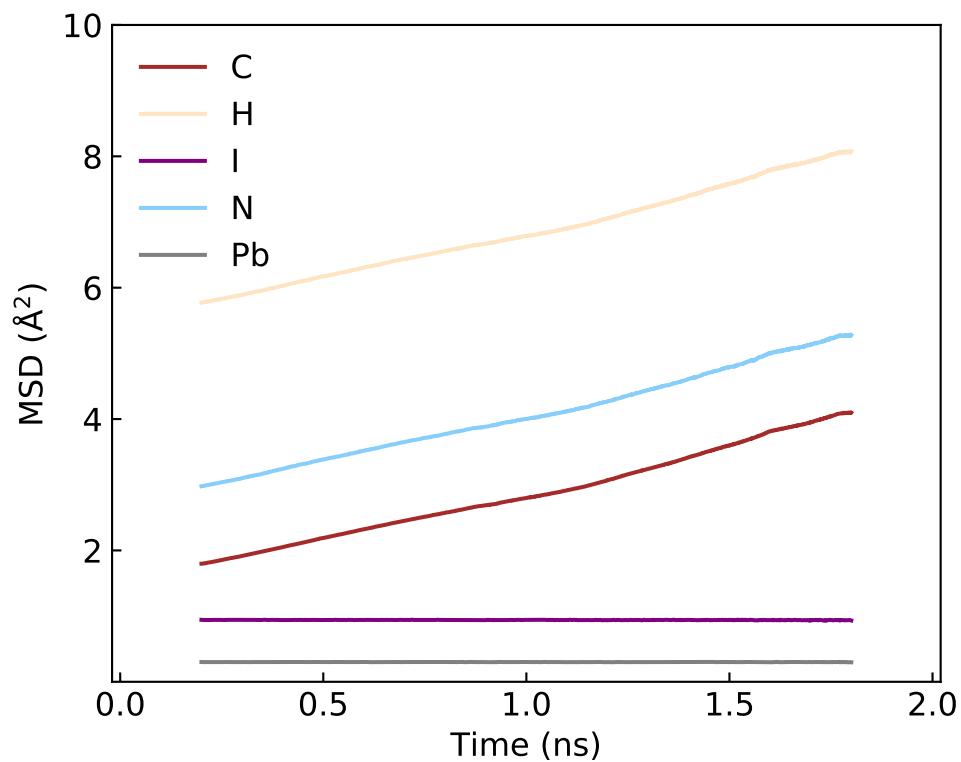


Figure S10: Mean squared displacement (MSD) curves decomposed to the atomic species over simulation time for I_{MA}^+ in $MAPbI_3$ at 550 K.

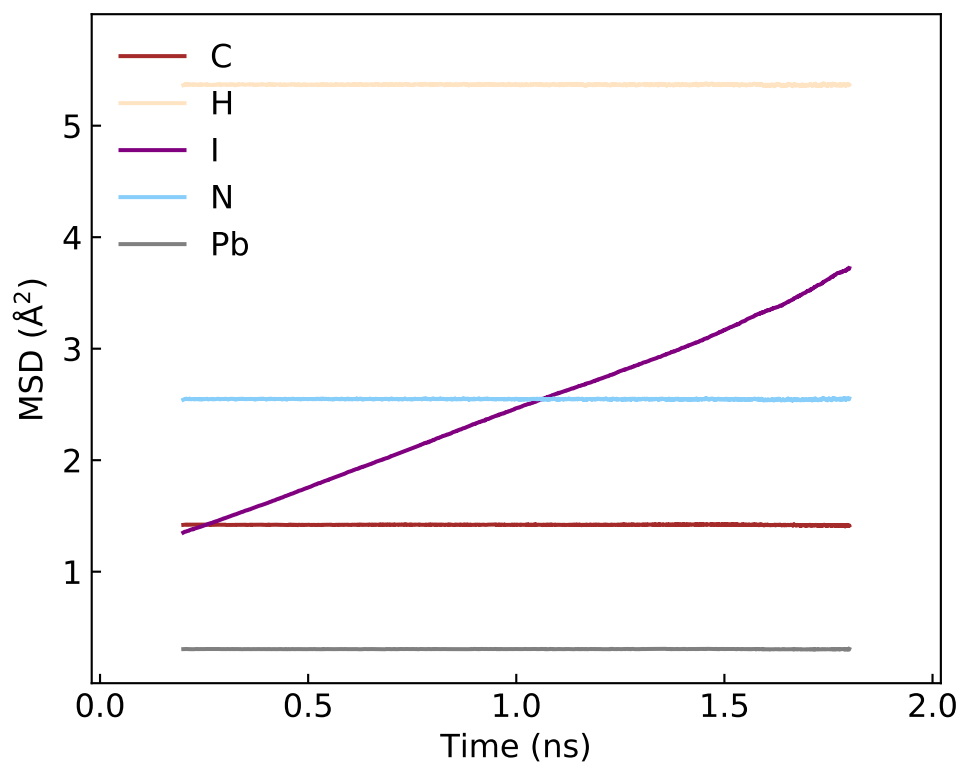


Figure S11: Mean squared displacement (MSD) curves decomposed to the atomic species over simulation time for I_1^- in $MAPbI_3$ at 550 K.

5 Charge density analysis

To check the charge distribution of the extra electron in I_{MA}^0 , its charge density is compared with that of its positive counterpart. The charge densities of the neutral and positive charge states are calculated using the optimized geometry of I_{MA}^0 . The difference between the charge densities is visualized in VESTA,²³ and is given in Figure S12. As evident from the figure, the extra electron delocalizes over the whole lattice.

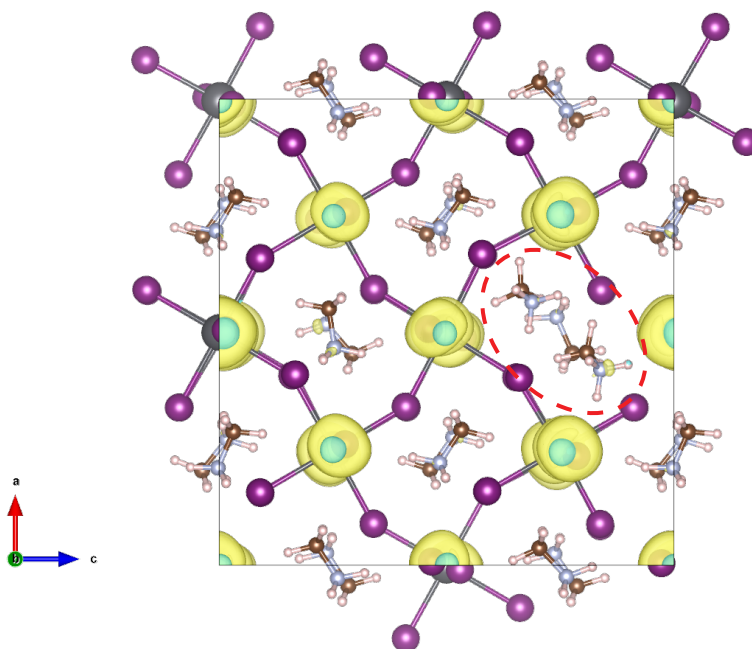


Figure S12: The charge density difference between the I_{MA}^0 and I_{MA}^+ , in the optimized geometry of I_{MA}^0 . The regions with a negative charge are colored in yellow, and the regions with a positive charge are colored in blue. The defect environment is circled in dotted red lines.

References

- (1) Kresse, G.; Furthmüller, J. Efficient iterative schemes for ab initio total-energy calculations using a plane-wave basis set. *Phys. Rev. B* **1996**, *54*, 11169–11186.
- (2) Jinnouchi, R.; Karsai, F.; Kresse, G. On-the-fly machine learning force field generation: Application to melting points. *Phys. Rev. B* **2019**, *100*, 014105.
- (3) Jinnouchi, R.; Lahnsteiner, J.; Karsai, F.; Kresse, G.; Bokdam, M. Phase Transitions of Hybrid Perovskites Simulated by Machine-Learning Force Fields Trained on the Fly with Bayesian Inference. *Phys. Rev. Lett.* **2019**, *122*, 225701.
- (4) Bartók, A. P.; Payne, M. C.; Kondor, R.; Csányi, G. Gaussian Approximation Potentials: The Accuracy of Quantum Mechanics, without the Electrons. *Phys. Rev. Lett.* **2010**, *104*, 136403.
- (5) Bartók, A. P.; Kondor, R.; Csányi, G. On representing chemical environments. *Phys. Rev. B* **2013**, *87*, 184115.
- (6) Parrinello, M.; Rahman, A. Crystal Structure and Pair Potentials: A Molecular-Dynamics Study. *Phys. Rev. Lett.* **1980**, *45*, 1196–1199.
- (7) Parrinello, M.; Rahman, A. Polymorphic transitions in single crystals: A new molecular dynamics method. *J. Appl. Phys.* **1981**, *52*, 7182–7190.
- (8) Kresse, G.; Joubert, D. From ultrasoft pseudopotentials to the projector augmented-wave method. *Phys. Rev. B* **1999**, *59*, 1758–1775.
- (9) Sun, J.; Ruzsinszky, A.; Perdew, J. P. Strongly Constrained and Appropriately Normed Semilocal Density Functional. *Phys. Rev. Lett.* **2015**, *115*, 036402.
- (10) Sabatini, R.; Gorni, T.; de Gironcoli, S. Nonlocal van der Waals density functional made simple and efficient. *Phys. Rev. B* **2013**, *87*, 041108.

- (11) Lahnsteiner, J.; Kresse, G.; Heinen, J.; Bokdam, M. Finite-temperature structure of the MAPbI₃ perovskite: Comparing density functional approximations and force fields to experiment. *Phys. Rev. Mater.* **2018**, *2*, 073604.
- (12) Bokdam, M.; Lahnsteiner, J.; Ramberger, B.; Schäfer, T.; Kresse, G. Assessing Density Functionals Using Many Body Theory for Hybrid Perovskites. *Phys. Rev. Lett.* **2017**, *119*, 145501.
- (13) Xue, H.; Brocks, G.; Tao, S. First-principles calculations of defects in metal halide perovskites: A performance comparison of density functionals. *Phys. Rev. Mater.* **2021**, *5*, 125408.
- (14) Monkhorst, H. J.; Pack, J. D. Special points for Brillouin-zone integrations. *Phys. Rev. B* **1976**, *13*, 5188–5192.
- (15) Batzner, S.; Musaelian, A.; Sun, L.; Geiger, M.; Mailoa, J. P.; Kornbluth, M.; Molinari, N.; Smidt, T. E.; Kozinsky, B. E(3)-equivariant graph neural networks for data-efficient and accurate interatomic potentials. *Nat. Comm.* **2022**, *13*, 2453.
- (16) Musaelian, A.; Batzner, S.; Johansson, A.; Sun, L.; Owen, C. J.; Kornbluth, M.; Kozinsky, B. Learning local equivariant representations for large-scale atomistic dynamics. *Nat. Comm.* **2023**, *14*, 579.
- (17) Tyagi, V.; Pols, M.; Brocks, G.; Tao, S. Tracing Ion Migration in Halide Perovskites with Machine Learned Force Fields. *J. Phys. Chem. Lett.* **2025**, *16*, 5153–5159.
- (18) Henkelman, G.; Uberuaga, B. P.; Jónsson, H. A climbing image nudged elastic band method for finding saddle points and minimum energy paths. *J. Chem. Phys.* **2000**, *113*, 9901–9904.
- (19) Whitfield, P. S.; Herron, N.; Guise, W. E.; Page, K.; Cheng, Y. Q.; Milas, I.; Crawford, M. K. Structures, Phase Transitions and Tricritical Behavior of the Hybrid Perovskite Methyl Ammonium Lead Iodide. *Sci. Rep.* **2016**, *6*, 35685.

- (20) Thompson, A. P.; Aktulga, H. M.; Berger, R.; Bolintineanu, D. S.; Brown, W. M.; Crozier, P. S.; in 't Veld, P. J.; Kohlmeyer, A.; Moore, S. G.; Nguyen, T. D. et al. LAMMPS - a flexible simulation tool for particle-based materials modeling at the atomic, meso, and continuum scales. *Comp. Phys. Comm.* **2022**, *271*, 108171.
- (21) Michaud-Agrawal, N.; Denning, E. J.; Woolf, T. B.; Beckstein, O. MDAAnalysis: A toolkit for the analysis of molecular dynamics simulations. *J. Comput. Chem.* **2011**, *32*, 2319–2327.
- (22) Maginn, E. J.; Messerly, R. A.; Carlson, D. J.; Roe, D. R.; Elliot, J. R. Best Practices for Computing Transport Properties 1. Self-Diffusivity and Viscosity from Equilibrium Molecular Dynamics [Article v1.0]. *LiveCoMs* **2018**, *1*, 6324.
- (23) Momma, K.; Izumi, F. VESTA: a three-dimensional visualization system for electronic and structural analysis. *J. Appl. Crystallogr.* **2008**, *41*, 653–658.